scientific reports

Check for updates

OPEN

Non-destructive detection of critical defects in additive manufacturing

Shaharyar Baig[1,2], Alireza Jam[1,2], Stefano Beretta[1,2,3], Shuai Shao[1,2] & Nima Shamsaei[1,2]✉

Non-destructive examination (NDE) based structural integrity assessment of additively manufactured (AM) metallic parts depends on the reliable detection of volumetric defects and the accurate representation of their detrimental features. Failure to detect critical defects and their features during NDE can result in dangerous non-conservativeness in fatigue design and part qualification, leading to dire engineering consequences. This work highlights an often overlooked property of X-ray computed tomography (XCT) in prevailing NDE practices, i.e., the dependence of the XCT efficacy on the shape of defects within a population, which can manifest in both the probability of their detection and the errors in characterizing their features. By examining an identical material volume of laser powder bed fused AlSi10Mg with XCT at different combinations of voxel size and coupon geometry, it is shown that the performance of XCT deteriorates more significantly for irregular-shaped defects, since their fine features tend to be lost. An approach to recover some important feature information of these irregular defects, such as size, using a distance-based criterion is proposed and is shown to enhance the sizing accuracy of these defects.

Volumetric defects, such as lack-of-fusions (LoFs), gas entrapped pores (GEPs), and keyholes (KHs), are well known be detrimental to the fatigue resistance of certain additively manufactured (AM) alloys, such as AlSi10Mg, Ti–6Al–4V, and 17-4 PH stainless steel, etc[1–5]. These defects are sites of stress concentration and, under cyclic loading, can result in accelerated fatigue crack initiation[6]. Accordingly, any variations in their characteristics that affect the stress concentration, such as size, shape, and location, can impact the extent of such acceleration and introduce significant uncertainty in the fatigue behavior of AM parts[7,8]. Therefore, non-destructive examination (NDE) techniques that can accurately reveal the internal defect structure within the parts can provide valuable information regarding their quality and are highly desirable[9–11]. With accurate defect-sensitive fatigue models, such defect information can be used to indicate the life of AM parts under service loads and accelerate their qualification by reducing the need for extensive campaigns of destructive testing at both coupon and part scales[12,13].

Among various NDE techniques, X-ray computed tomography (XCT) stands out due to its unique ability to detect volumetric defect features at micrometer and sub-micrometer levels of physical resolution[14,15]. Nevertheless, XCT is relatively time consuming and, due to constrains imposed by the X-ray attenuation within materials and the pixel count of the optical sensors, is well known to suffer from the tradeoff between resolution and the scanned volume[16]. Generally, fine physical features are more challenging to be resolved in a larger part, because each voxel must register larger spatial volume for larger format scans and the X-ray attenuation is more severe in thicker materials, deteriorating the signal-to-noise ratio[14,17,18]. While employing higher voltage sources can increase X-ray transmittance, it does not necessarily improve resolution, since the X-ray beam spot size typically increases with increasing voltage which adversely affects imaging quality[17]. Accordingly, in an industrial setting, where large quantities of AM parts (likely large in size) need to be scanned in limited time, the resolution achieved by the XCT scans is often not ideal.

At a reduced scan resolution, the imaging contrast of fine geometrical features whose size approaches or falls below the size of a voxel may become indistinguishable from that of the noise, leading to detection failures[19]. These geometries can be the entirety of small GEP (see Fig. 1a) or parts of a larger defect, such as the thin webbings in a LoF (see Fig. 1b). This implies that the probability of detection (POD) of defects, especially small ones, therefore markedly declines with the decreasing resolution. Large defects, although their POD may be less sensitive to resolution, can be significantly misrepresented by XCT scans at low resolutions, depending on their shape[20]. However, KHs are near spherical, generally lack features that extend far from their bulks[21], and

[1]National Center for Additive Manufacturing Excellence (NCAME), Auburn University, Auburn, AL 36849, USA. [2]Department of Mechanical Engineering, Auburn University, Auburn, AL 36849, USA. [3]Department of Mechanical Engineering, Politecnico di Milano, Milan 20156, Italy. ✉email: shamsaei@auburn.edu

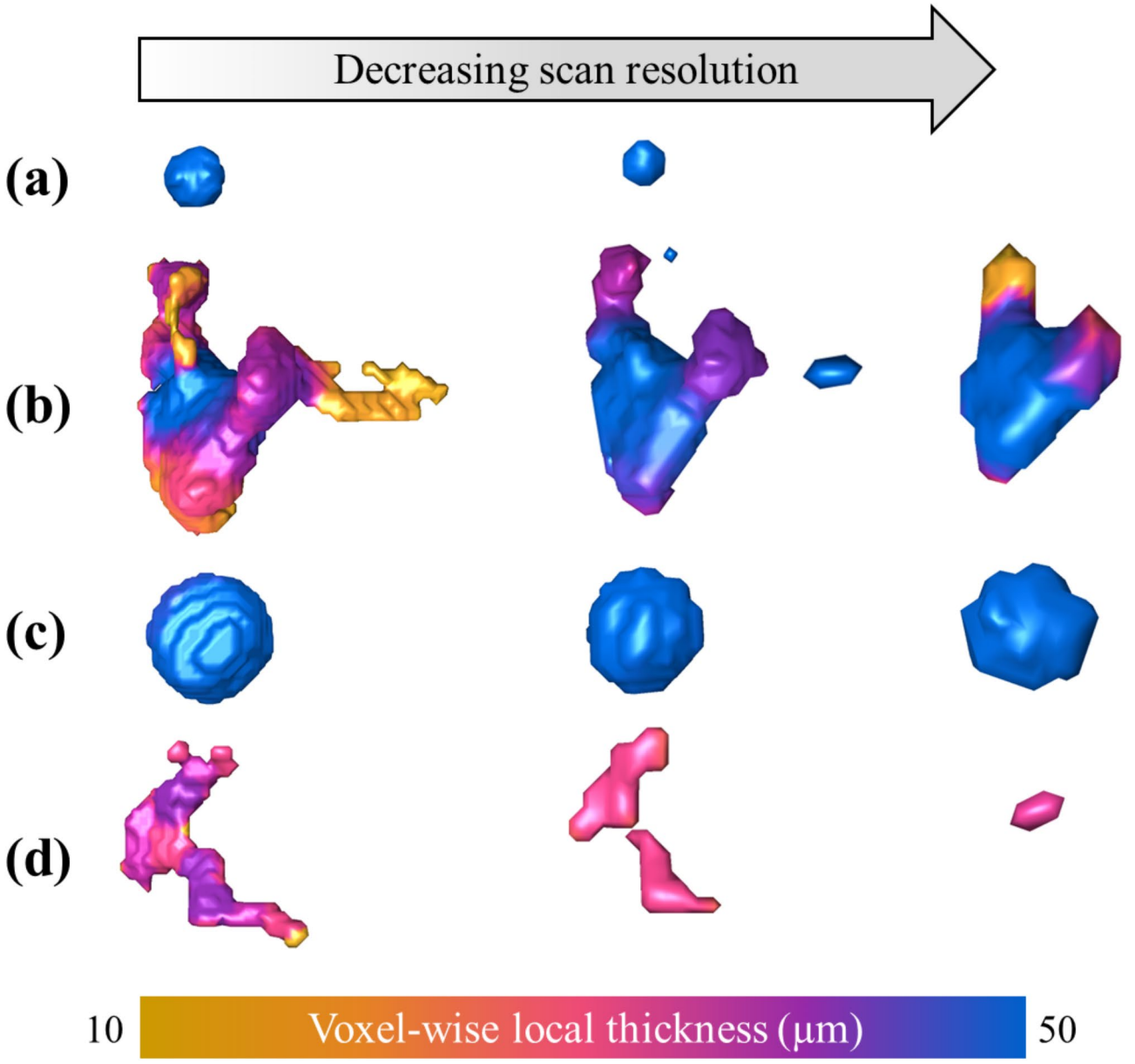

Fig. 1. The influence of XCT scanning resolution on the detected morphology of various types of defects. The defect types shown are: (**a**) GEP, (**b**) LoF consisting of thin webbings extending out of a single bulky region, (**c**) KH, and (**d**) LoF with less bulky features.

can be captured by the low-resolution scans with good reliability if they are several times larger than a voxel (see Fig. 1c). On the other hand, LoFs are irregularly shaped and typically comprise thicker, bulkier regions and thin webbings (see Fig. 1b). At reduced resolutions, while the bulkier regions can still be captured by the scans, the thin webbings tend to be missed. As a result, a large LoF defect may appear as one or a few smaller defects and, accordingly, its size can be severely underestimated[22]. In some extreme cases, LoFs appear as only a few disconnected, globular features and are missed by the scans altogether (see Fig. 1d).

As such, the efficacy of an XCT system in detecting volumetric defects, i.e., *the POD*, and in determining their sizes and other geometrical features, i.e., *feature errors*, can be significantly dictated by the shapes of defects within their population[23–27]. This study aims to evaluate the quality of XCT scans by quantifying the POD and the feature errors with differentiating defects' geometry. Moreover, it devises a methodology to improve the accuracy of lower-quality scans in estimating the size of volumetric defects, especially larger LoFs. The focus of this study is on the characterization of process-induced volumetric defects which are inherently challenging to avoid due to the nature of the AM process, even in machined parts free of any surface anomalies. Different levels of scan quality are achieved by XCT scanning an identical, laser powder bed fused (L-PBF) AlSi10Mg material volume multiple times at different coupon diameters (10, 6, and 3 mm) and voxel sizes (10.8, 6.4 and 3.4 μm) in a factorial experiment. The AlSi10Mg coupon is fabricated with a set of process parameters to induce all three

types of volumetric defects, i.e., LoFs, GEPs, and KHs. The examination of the identical material volume permits the true one-to-one comparison of the same volumetric defects across different acquisition conditions. It is shown that both POD and feature errors are indeed significantly influenced by the types of defects within the material volume. Although the finer features of a LoF, i.e., webbings, tend to be lost as the scan quality reduces, certain critical information, such as its size, can be partially recovered as long as a few of its bulkier regions can be captured and identified by applying a distance-based criterion, established in this research.

Results

Assessing the quality of XCT scans—probability of detection (POD)

Conventionally, the quality of an XCT scan is quantified by the POD of a defect as a function of some measure of the defect's size, regardless of its shape[28]. The POD is obtained from the hit/miss defect analysis performed on a sample whose ground truth information about its defect population is known and is typically presented as a sigmoid POD curve[29,30]. The hit/miss analysis was performed using a defect detection algorithm that enabled one-to-one matching of defects between the low-resolution scans and the ground truth. A defect was flagged as a hit if it was detected within the bounding box volume of the ground truth defect; otherwise, it was flagged as a miss if no detection occurred. The POD curves for all defects, regardless of their geometry, along with their 95% confidence intervals are shown in Fig. 2 in black lines and gray shades for the XCT scans performed on the AlSi10Mg coupon at different permutations of voxel sizes and coupon diameters. The permutations are designated by the convention "*voxel size-coupon size*", e.g., 3 µm–6 mm represents a 3.4 µm-voxel scan on a 6 mm-diameter coupon. The $\sqrt{area}$ parameter was selected to represent defects' size since it has been shown to correlate well with fatigue criticality[22,31]. In this work, the projection plane for the size measurements was selected to be the one perpendicular to the build direction. To avoid false detection of volumetric defects from noise, the decision threshold was set to a $\sqrt{area} \geq 2$ voxels, i.e., any defects that appeared smaller than this size are flagged "missed" (see Fig. S3 in Supplemental Materials showing the effect of noise threshold on POD). In

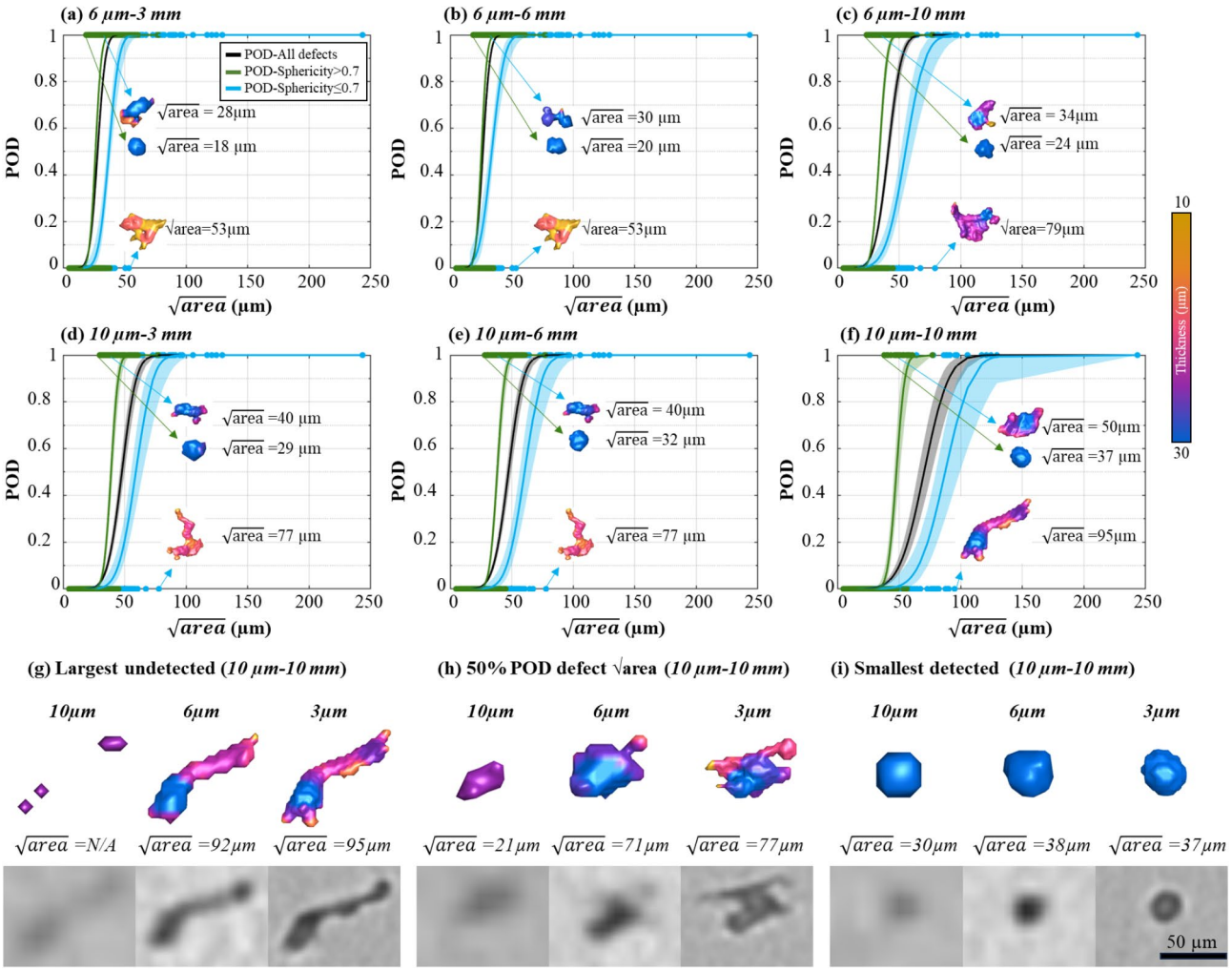

Fig. 2. (**a**–**f**) POD curves for various voxel/coupon size scans and for different defect classes based on their sphericity values, and (**g**–**i**) visualization of the largest undetected, 50% POD defect $\sqrt{area}$ and smallest detected defects in the 10 µm–10 mm scan.

the case of multiple small features of a large LoF being detected, a positive detection was registered if at least one feature exceeded the decision threshold size. Additionally, the sizes of all the missed and detected defects are shown in this figure as markers on the lines of POD = 0 and POD = 1, respectively. It should be noted that, with the 3 µm–3 mm scan as the ground truth, all of the defects were detected in the 3 µm–6 mm and 3 µm–10 mm scans; in these cases, the POD curves appear as vertical lines at $\sqrt{area}$ = 6 µm and are therefore not presented here.

The figure shows that and the POD curve clearly shifted towards larger $\sqrt{area}$ with increasing voxel size (compare the black curves in Fig. 2a–c with the ones in Fig. 2d–f). Moreover, the coupon size also have influenced the POD, with larger coupons having right-shifted POD curves[17]. In addition to the POD itself, the uncertainty of the POD (represented by the width of the confidence bands shown by the shaded regions) also increased with voxel size and coupon diameter. The ground truth of the largest missed and smallest detected defects for each voxel/coupon size combination is also visualized in each panel, with arrows pointing the corresponding datapoints to the defect's visual representation, and their reported $\sqrt{\text{area}}$s. Evidently, the largest undetected defect was always a LoF and the smallest detected one was always spherical (could be a KH or GEP) in all scans, and the former were always significantly larger than the latter. For instance, the largest undetected defect in the 10 µm–10 mm scan was a LoF and had a $\sqrt{area}$ = 95 µm; the smallest detected one in the same scan was near-spherical and had a $\sqrt{area}$ = 38 µm. The stark contrast between the size of the largest undetected/smallest detected defects suggested that the POD depends on the shape of the defects and should be quantified separately for each defect type[32].

To further elucidate how the defects' shape may affect POD, the defects were divided into two categories according to their type, i.e., near-spherical (comprising KHs and GEPs with sphericity values > 0.7) and irregular (comprising LoFs only with sphericity values ≤ 0.7)[33]. The classification of defects into KHs, GEPs, and LoFs was achieved following the automatic approach set forth by the authors' prior work and was verified by manually inspecting the classified defects to ensure they were appropriately assigned to their respective classes[34]. The two additional POD curves of near-spherical and irregular defects for each set of acquisition parameters are presented in Fig. 2 in green and blue with shades of the corresponding colors. For defects of size up to ~10 voxels, it appeared that the POD for irregular defects (blue curves) was lower than those for near-spherical ones (green curves) and when considering all defects in the scan volume indiscriminately (black curves). In addition, the gently sloping POD curves of the irregular defects also implied that the POD gradually improves with an increase in the defect size. This was opposed to the behavior of the near-spherical defects gaining high detectability once their size approached the decision threshold, which was set as $\sqrt{area} \geq 2$ voxels in this study. The observation held true for all the acquisition parameters investigated in this study and was more pronounced at the 10 µm voxel size and for the 10 mm coupon diameter, as observed in Fig. 2c–f. Furthermore, the uncertainties associated with the POD of near-spherical defects were significantly lower than the irregular ones and remained relatively unchanged with an increase in voxel/coupon size (compare the widths of the green and blue shades in Fig. 2).

The shallower and more uncertain POD curves of LoFs than those of near-spherical defects (including GEPs and KHs) originated from the strong variability of LoFs' shape[35]. On one hand, some LoFs comprised only thin features, which tended to be lost with the deteriorating imaging quality which was the case for the largest undetected defects in all acquisition conditions (see the ones visualized in each panel of Fig. 2c–f). As an example, the appearances of one of such LoFs (i.e., the largest undetected defect in the 10 µm–10 mm scan) in the 3 µm–3 mm (ground truth), 6 µm–6 mm, and 10 µm–10 mm scans, are visualized in Fig. 2g alongside the corresponding gray scale images. It is evident from the figure that, as the resolution reduces, the fine features of this serpentine shaped defect became gradually indistinguishable from noise, such that in the 10 µm–10 mm scan only a cluster of small entities could be segmented. Since all of them fell below the decision threshold (i.e., 2 voxels), the defect was recorded as undetected.

On the other hand, some LoFs contained at least one bulky region and, despite the loss of thin webbing to reduced scan resolutions, could still be relatively reliably detected (see the smallest detected LoFs visualized in Fig. 2c–f). One example of this case (i.e., a defect of a $\sqrt{area}$ equivalent to 50% POD in the 10 µm–10 mm scan) is illustrated in Fig. 2h, following the format used for Fig. 2g. In contrast, near-spherical defects generally lacked thin features and could be detected as long as the size of the segmented objects is above the decision threshold of 2 voxels (see Fig. 2i, which shows the smallest detected defect in the 10 µm–10 mm scan). The POD of a near-spherical defect was influenced by both the morphology of the defects and the level of noise within the images. Larger, more spherical defects could be reliably detected, even in the lower-resolution scans. For smaller defects whose shape deviated from a sphere and had $\sqrt{\text{area}}$s approaching the decision threshold, the POD was impacted by the image noise more significantly, as the quality of XCT scans degraded.

Assessing the quality of XCT scans—feature errors

While the quantification of the POD presents valuable information regarding the reliability of the XCT examination in detecting a defect of a given size, it does not account for the errors in the measurements of their features, such as size[18,36]. Depending on the acquisition parameters used for the XCT inspection, the detected features may vary drastically for the same defects, resulting in large errors in the feature measurements[18]. This could be due to several factors such as the loss of information as the voxel size increases and the lower signal-to-noise ratio as the part size increases which may result in fine features not being captured fully[37]. As a result of the lost fine features, defect populations acquired with lower resolutions typically contained smaller and rounder defects when compared to the ground truth, as shown in the sphericity versus $\sqrt{\text{area}}$ plots presented in Figs. S1 and S2 of the Supplemental Material.

The measured versus ground truth $\sqrt{area}$ for the various scans performed with different acquisition parameters are plotted in Fig. 3. Note, again, that the 3 µm–3 mm scan was used as the ground truth. Here, the

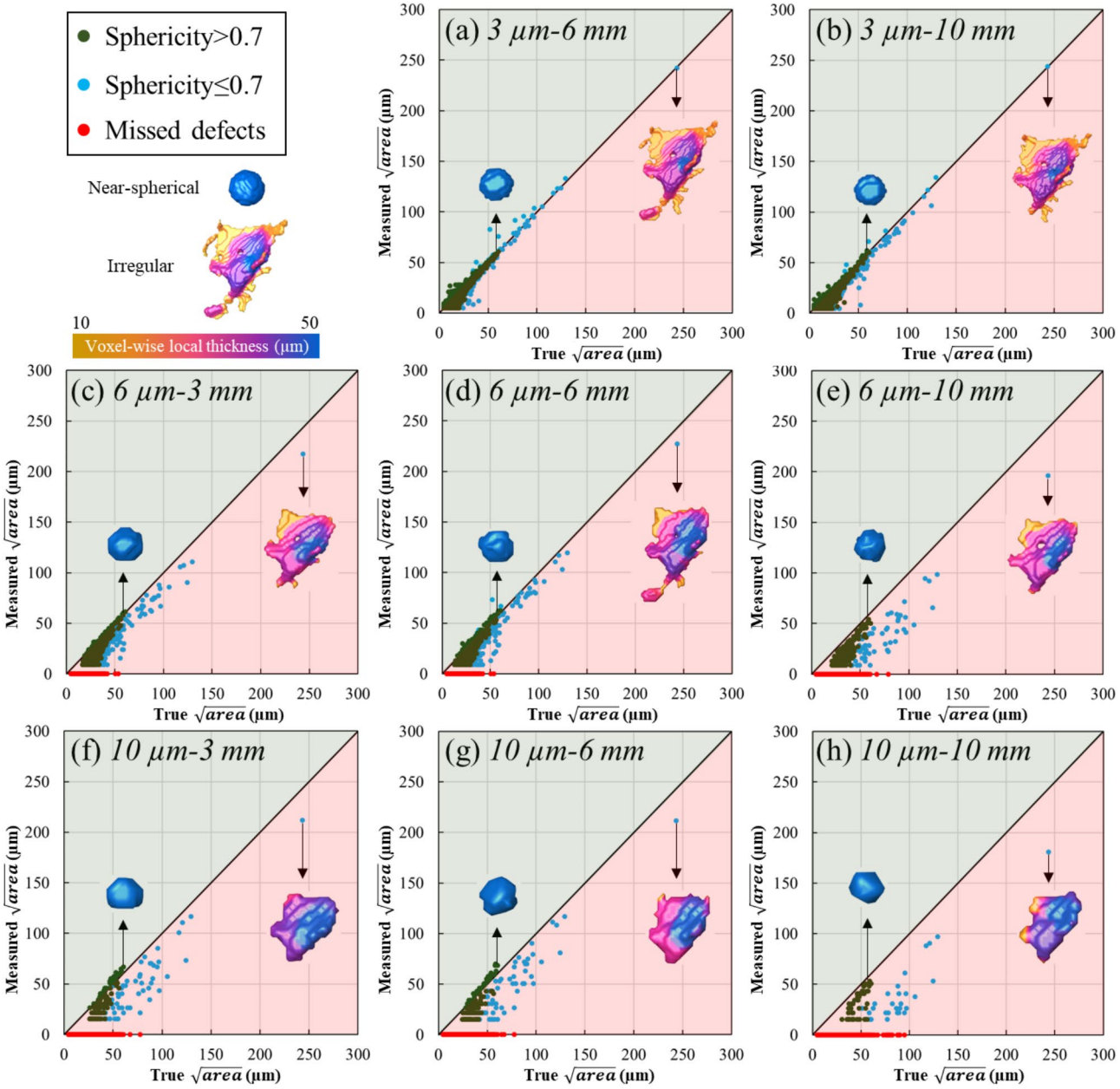

Fig. 3. Measured versus true $\sqrt{area}$ for all matched defects across various voxel/coupon size scans. The true size was obtained from the 3 μm–3 mm scan.

measured areas were calculated by summing up the areas of all the entities detected inside the bounding box of the corresponding ground truth defect. The black diagonal line in the figures represents the 1:1 identity. The defects that were not detected by XCT scans, i.e., the missed ones presented in Fig. 2, correspond to "0" $\sqrt{area}$ and are shown with the red markers on the horizontal axis. The measured sizes appeared to be strongly affected by the voxel size. For instance, the scans with 3 μm voxel (i.e., the same voxel size as the 3 μm–3 mm ground truth scan) measured the $\sqrt{area}$ with the highest fidelity. As the voxel size increased to 6 μm, the $\sqrt{area}$ was underestimated for most defects. The irregular defects with low sphericity values appeared to be underestimated more significantly than the near-spherical. Interestingly, increasing the voxel size to 10 μm only worsened the underestimation for the irregular defects further and did not significantly affect the sizing errors for the near-spherical ones. Moreover, some influence of the part size on the measured $\sqrt{area}$ was also observed, especially at the largest coupon sizes of 10 mm where the errors were more pronounced for voxel sizes of 6 and 10 μm.

The appearances of one near-spherical and one irregular defect, the latter's size tends to be consistently underestimated by XCT scans, with all acquisition parameters are visualized in each panel of Fig. 3, and their appearance in the ground truth scan are provided in upper left of the figure. The near-spherical defect, whose size was measured to be close to the ground truth size and remained relatively unchanged with changes in acquisition

parameters, showed a round morphology in all scans. This defect had a local thickness of ~ 50 µm, lacked any features extending from its spherical core region, and was reliably captured in XCT scans at all resolutions.

In contrast, the LoF consisted of thin webbings (shown in blue in the top left panel of Fig. 3) extending out of a bulkier region (shown in yellow). In this case, the local thickness of the defect had a significant influence on the detectability of its features in the lower-resolution scans. For instance, in the 3 µm–6 mm and 3 µm–10 mm scans, all features of the defect were detected including the thin webbed regions, which resulted in the measured $\sqrt{area}$ being in close agreement with the ground truth. However, as the voxel size increased to 6 µm, some features with low thickness values could not be captured. At the voxel size of 10 µm, a significant portion of the LoF could not be captured, and only the bulky core region was detected resulting in a severe underestimation of the defect size. Moreover, the loss of feature information for the LoF was further exacerbated by an increase in coupon size, and the most severe underestimation was seen for the 10 mm coupon size at both 6 and 10 µm voxel sizes.

Reducing feature errors—applying distance criterion

The sizing error in $\sqrt{area}$ was the most significant for the irregular defects (i.e., the LoFs), which stemmed from their fine features being missed due to the resolution limitations. Although the thin webbings could not be detected and the LoFs appeared as a cluster of entities at reduced resolutions, the convex hull constructed around these entities should better represent the $\sqrt{area}$ of the LoF, if the registry of these entities to the LoF defect could be established. Based on this understanding, a procedure, "polygonization approach", was devised to reduce the sizing error of irregular defects. The procedure began with identifying a few (approximately 20) larger and more critical LoFs from the ground truth whose appearance changed to at least two isolated, small entities in the lower-resolution scans. Figure 4 illustrates the proposed polygonization procedure using one LoF as an example. For each LoF at each resolution (see Fig. 4a,b), the largest pairwise, centroidal distance (d) among the entities was measured. Then, at each resolution, the greatest d value calculated for the limited number of LoFs (~ 20) was set as the distance threshold (Fig. 4c). This threshold was used to examine all clusters of small entities detected at that resolution to determine if they belonged to the same large LoFs by blindly applying to the entire dataset for the low-resolution scan (Fig. 4d). With this approach, the recovery of critical defect information from scans on relatively large parts, whose resolution is often less than ideal, may be possible as long as the threshold distances for the volumetric defects in the same material with increasing part size and voxel size is established based on limited ground truth information.

The measured versus. true $\sqrt{area}$ plots are presented in Fig. 5, after applying the distance criterion to construct the convex hull using the bounding boxes of the clustered entities and recalculating the $\sqrt{area}$s. In addition, the number of defects with two or more bulky regions (Poly) in the low-resolution scans, which the polygonization approach was able to improve the sizing accuracy for, are reported in the bottom right side of each panel along with the number of defects which only had singular bulky regions (Single), The measured values appeared to significantly improve, especially for the larger defects, despite the size for some defects being overestimated. The overestimation was acceptable as they would lead to a more conservative assessment of the fatigue resistance.

To further understand the effectiveness of the proposed polygonization approach in improving the $\sqrt{area}$ measurements for various irregular defects, three representative LoFs were selected for further examination. The markers for the three defects have been numbered in Fig. 5 for easy comparison. The 3D renderings of

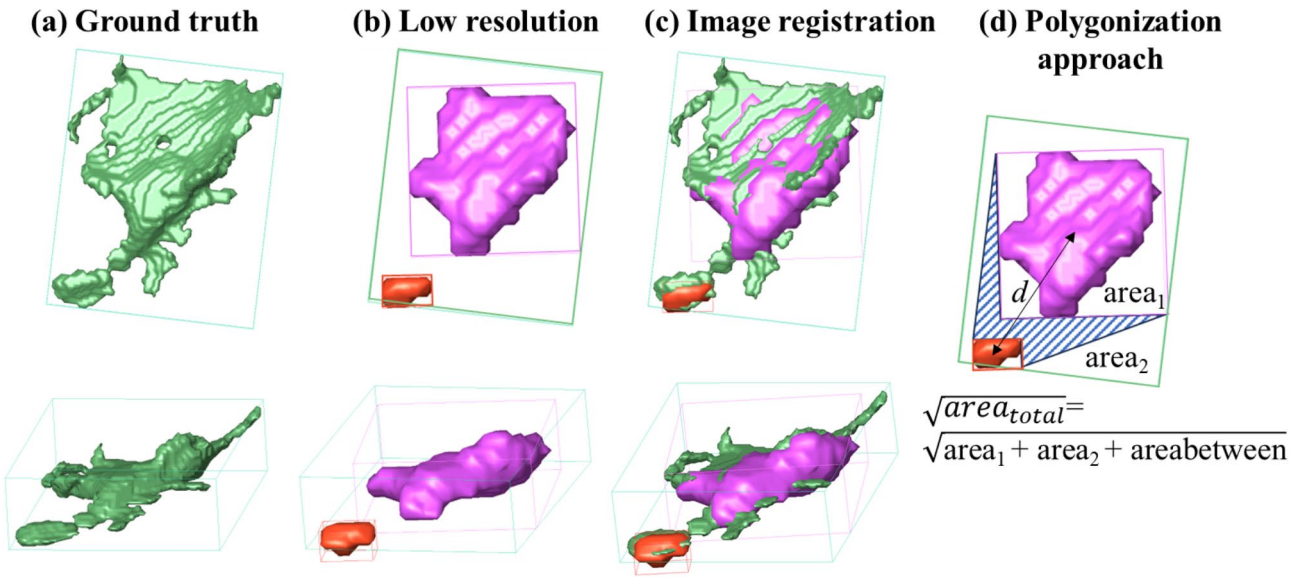

Fig. 4. (**a**) Ground truth defect, (**b**) corresponding entities detected in the low resolution scans, (**c**) defect matching between the ground truth and low resolution scan based on the bounding boxes, and (**d**) polygonization approach considering the area in between the defects.

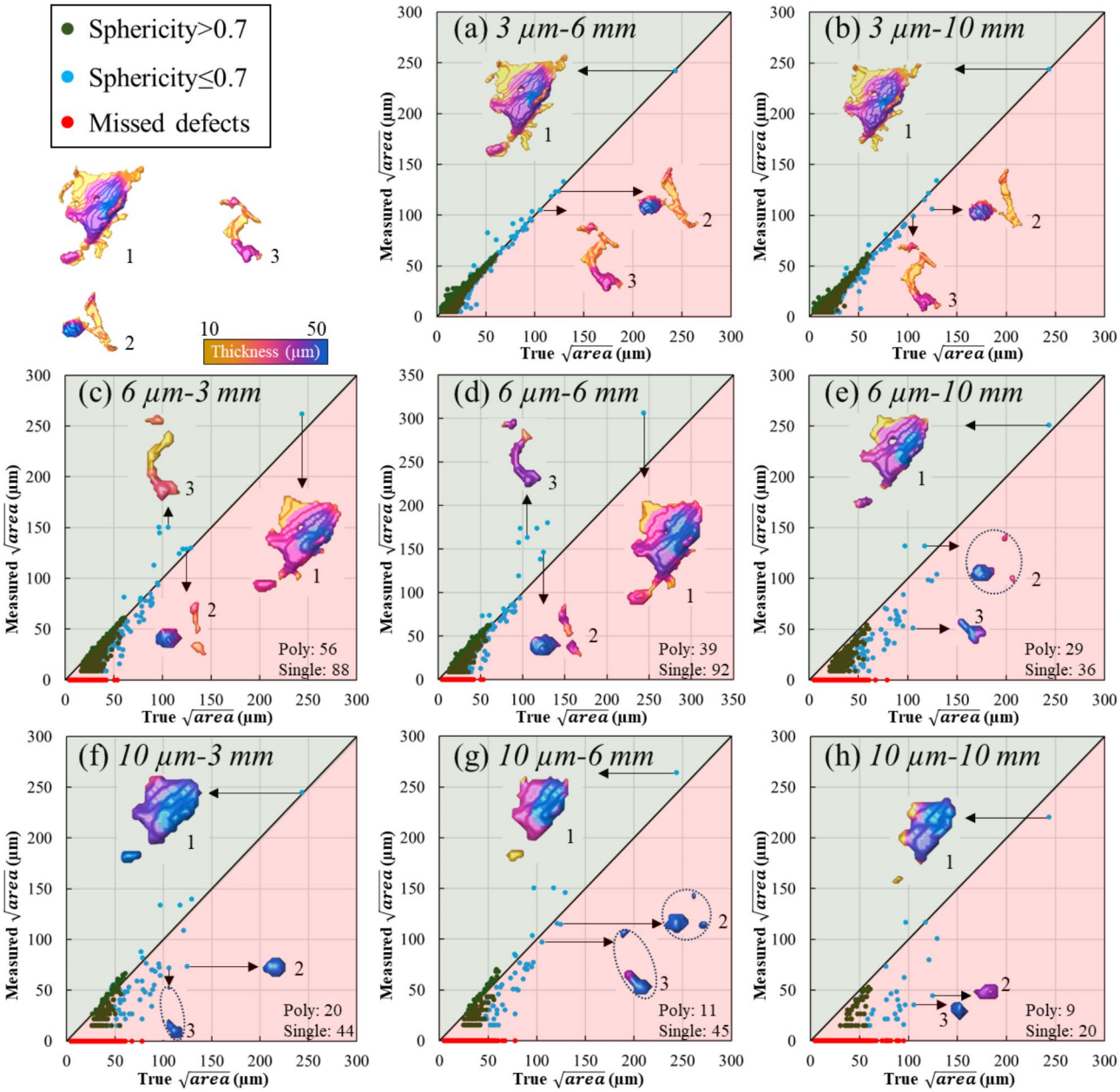

Fig. 5. Measured versus true $\sqrt{\text{area}}$ considering the distances between neighboring defects and applying polygonization procedure for any defects within the distance thresholds. The number of defects with two or more bulky regions (Poly) are also listed along with the number of unmodified defects with singular bulky regions (Single). The true size was obtained from the 3 μm–3 mm scan.

the defects are presented in Fig. 5, with the ground truth shown in the top left of the figure and the detected morphologies for each acquisition parameter visualized on the measured versus true $\sqrt{area}$ plots. For Defect 1, which was the largest defect in the dataset and whose size was underestimated in the 6 μm and 10 μm scans (see Fig. 3), applying the polygonization procedure improved the measured $\sqrt{area}$, resulting in significantly reduced errors (Fig. 5) and, in some cases, slight overestimation into conservativeness. As the scan resolution decreased with an increase in the voxel size from 3 μm to 6 μm and 10 μm and with an increase in coupon size from 3 mm to 6 mm and 10 mm, Defect 1 "disintegrated" into a cluster of a large and a small entity. Since both could be consistently detected in all acquisition conditions, Defect 1's $\sqrt{area}$ was adequately captured by constructing the convex hull around the bounding boxes of these entities.

In contrast, for Defects 2 and 3, the polygonization procedure was only effective in some of the scans. This included all scans conducted at the 6 μm voxel size and the 10 μm–6 mm scan for Defect 2, and 6 μm–3 mm, 6 μm–6 mm, 10 μm–3 mm and 10 μm–6 mm scans for Defect 3. As is evident in the ground truth images in Fig. 5, Defects 2 and 3 each contains only one bulky region and some thinner webbed features. In certain acquisition conditions of reduced resolution, the webbed features were lost and only the singular bulky region

of each defect was detected, which was insufficient for the convex hull to be constructed. Indeed, the acquisition conditions where the procedure showed improvement in the measured $\sqrt{area}$ were the ones that successfully captured multiple entities for each defect. For example, defect 2 saw a large improvement in the measured $\sqrt{areas}$ for most scan parameters and was captured as 3 separate entities in all of 6 µm voxel size scans and in the 10 µm–6 mm scans. However, only the bulky region of the defect was detected in the 10 µm–3 mm and 10 µm–10 mm. This could be attributed to the 10 µm–3 mm scan having a higher transmittance than the 10 µm–6 mm and 10 µm–10 mm scans which resulted in a lower contrast for defects closer to the specimen surface, which was the case for Defect 2 (see Fig. S4f–j) in the Supplemental Material)[38]. In addition, for the larger coupon diameters, the more severe attenuation of photons resulted in a poor signal-to-noise ratio and can explain the graininess and loss of features in the 10 µm–10 mm XCT images (see Fig. S4f–j in the Supplemental Material).

Discussion

This work demonstrated that the efficacy of XCT on AM parts and how it can degrade with deteriorating imaging conditions, such as increasing voxel size and/or part thickness, significantly depend on geometries of defects within their population. The efficacy not only manifests in the probability of detecting volumetric defects (see "Assessing the quality of XCT scans—probability of detection (POD)" Section) and but also in the accuracy in assessing defect features, such as size (see "Assessing the quality of XCT scans—feature errors" Section). While its general reducing trend with poorer imaging conditions is unavoidable and somewhat expected, the sensitivity of XCT scan's performance to the defect geometry has not been well known. The latter can negatively impact the outcome of the prevailing industrial practice of NDE based structural integrity assessment on AM parts, which does not emphasize on the effect of defects' shape[25–27,39]. Taking damage tolerant fatigue approaches for example, they estimate service life of a part by integrating crack growth laws from the initial crack size to the final crack size at fracture[23,24,40,41]. They always assume the presence of life limiting flaws within the materials and, for the initial crack size, use the detection limit of the NDE technique on the part/material combination of interest determined from the POD (e.g., defect size corresponding to 90% POD at a confidence level of 95%, see Fig. 2) even if no defects could be detected[22,42]. If the POD of an XCT system has been measured from an artifact predominantly containing near-spherical defects, such as KHs and GEPs, the calculated detection limit would be an underestimation if the part of interest contains predominantly LoFs. Since fatigue cracks' growth rate are much slower when they are short, such an underestimation in the initial crack size would significantly overestimate the part life, leading to dangerous, severely non-conservativeness in design[43,44].

If defects can be detected, on the other hand, assessing the structural integrity of AM parts via NDE hinges upon whether key attributes of the most detrimental defects can be accurately registered[39,45]. While the accuracy of XCT in capturing the size of the near-spherical defects has been shown adequate and is not strongly impacted by the imaging condition, as long as the defects can be detected, the sizing accuracy of XCT for LoFs deteriorates significantly with reducing imaging quality. Specifically, with only the smaller, bulkier regions captured, the size of the LoFs is underestimated, leading to overestimations of parts' service life by, for example, the damage tolerant fatigue approaches.

Recognizing the characteristics of a LoF often comprising more than one bulkier region which can be more reliably detected by XCT scans of reduced resolution (see Figs. 1 and 5), this work demonstrates that its size can be well represented by that of the convex hull constructed around these isolated regions, as long as their registry to the LoF can be established. With a set of threshold distance criteria to establish such registry, the overall sizing accuracy of XCT scans of reduced resolution for volumetric defects, especially the LoFs, has been shown to improve. Note that, given its working principle, this methodology is only effective for defects with a combination of a few bulky regions connected by thin features, e.g., large LoFs, and does not reduce sizing errors for defects with singular bulky features, e.g., KHs, GEPs, and smaller defects, or the ones without any bulkier regions, e.g., very small LoFs. In addition, it is a possibility that the procedure may combine two small spherical defects and consider them as a slightly larger entity if they fall within the distance thresholds, since it is not possible to distinguish between defects with a singular bulky region and a LoF with several bulky region in low resolution grayscale absorption images. Nevertheless, since the sizing error for the near-spherical defects is typically small and the small LoFs are typically not fatigue critical, the proposed approach is still expected to substantially benefit NDE based structural integrity assessment for AM parts despite these exceptions.

The proposed polygonization approach can help improve the compromised resolution of XCT imposed by part size, a challenge faced by many industrial radiographers. Specifically, important information regarding the critical defects' size in a relatively large AM part can be recovered from lower-resolution scans by understanding how defects' geometrical features are lost as scan resolution reduces. With a material sample excised from a similar part, this information and the threshold distance criteria can be obtained by XCT scans performed on the same material volume but at successively reducing coupon and voxel sizes.

Overall, although the results presented in this work, such as the POD curves and sizing error data, can potentially vary with material and acquisition setup, which affects the X-ray's attenuation and the resulting signal-to-noise ratio, the conclusions drawn should remain qualitatively valid for other AM materials/conditions. Specifically, process-induced volumetric defects such as KHs, GEPs, and LoFs are inherently present and characteristic of many families of AM metallic materials. Therefore, the importance in the consideration of the shape of volumetric defects within the industrial practice of NDE for AM parts highlighted in this work and proposed approach to improve the defects' sizing accuracy is expected to be applicable to many combinations of materials, fabrication techniques, and XCT imaging conditions.

In summary, this work investigated the influence of XCT acquisition parameters on the POD and feature errors with differentiating defect's geometry. Based on the results, the following conclusions were drawn:

- The POD for volumetric defects was significantly influenced by the shape of the defect. While near-spherical pores could be detected reliably across various XCT scanning conditions investigated in this study, the variability in the shape of LoFs resulted in a greater degree of uncertainty in their detection with worsening imaging quality.
- XCT accuracy in capturing defect features significantly deteriorated at reduced scan resolutions for LoFs due to a loss of information. This was attributed to the complex morphologies of LoFs which consisted of multiple bulky and webbed regions, with the latter having the most information loss associated with them. In contrast, the feature errors were relatively smaller for small LoFs, GEPs and KHs, which consisted of single bulky regions which could be adequately captured across various XCT scan resolutions.
- It is possible to recover some information from low resolution XCT scans for large critical LoFs with two or more bulky regions. By using a distance-based criterion to interpolate in between the bulky regions, the defect geometry could be reconstructed, allowing for enhanced sizing accuracy.

Methods

Fabrication and XCT scanning procedures

A cylindrical AlSi10Mg coupon (11 mm in diameter and ~45 mm in length) was fabricated on Renishaw RenAM500Q laser powder bed fusion system. Argon-atomized AlSi10Mg powder supplied by Renishaw was used as the feedstock and the quad-laser strategy working in a stripe pattern was adopted for fabrication. The recommended process parameters were employed which were able to induce LoFs, GEPs and KHs throughout the volume of the coupon. Post fabrication, the coupon was machined to a 10 mm diameter to remove any surface anomalies and to examine the internal porosity. The 10 mm coupon was XCT scanned at three different voxel sizes following the procedures described below. Afterwards, the coupon was further machined to diameters of 6 and 3 mm, and the scanning procedures were repeated according to the methodology described below at each step of the machining.

The XCT scans were performed using a Zeiss Xradia 620 Versa system. A total of 9 scans were conducted for various combinations of voxel/coupon sizes as presented in Fig. 6. Three different voxel sizes of 3.4, 6.3 and 10.8 µm were used to scan the coupon after each step of machining. These voxel and coupon size selections were made to ensure high quality imaging of the defect features found in L-PBF AlSi10Mg, while also considering certain constraints presented by scanning large AM components where the voxel size-part size tradeoff can make it necessary to scan AM parts at less than ideal resolutions in industrial settings. The voxel size was adjusted between the 6.3 and 10.8 µm by changing the source-to-sample-to-detector distances while keeping the objective lens of 0.4X identical. A lens of higher optical magnification of 4X was used for the 3.4 µm voxel size. For all the scans, a total number of 1600 projections were taken to maximize the likelihood of achieving the highest contrast view of the defects within a reasonable scan time. The transmittance for all scans was kept > 15%, while also considering the scan quality and the time to obtain high quality XCT images. The voxel size used in the "*voxel size-coupon size*" naming convention for the acquisition parameters was simplified by truncating the digits after the dot. For example, 6 µm–10 mm denoted the scan with the 6.3 µm actual voxel size, etc.

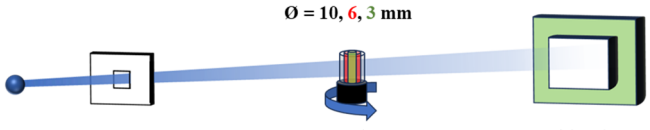

Specimen size	Voxel size=10.8 µm	Voxel size=6.3 µm	Voxel size=3.4 µm
10 mm	Voltage=70 kV Power=8.5 W Time=**2h** Obj=0.4x Transmit=22 %	Voltage=80 kV Power=10 W Time=**3h** Obj=0.4x Transmit=26 %	Voltage=100 kV Power=14 W Time=**9h** Obj=4x Transmit= 29%
6 mm	Voltage=60 kV Power=6.5 W Time=**2.5h** Obj=0.4x Transmit=28 %	Voltage=70 kV Power=8.5 W Time=**3h** Obj=0.4x Transmit=33 %	Voltage=100 kV Power=14 W Time=**9h** Obj=4x Transmit=39 %
3 mm	Voltage=60 kV Power=6.5 W Time=**2h** Obj=0.4x Transmit=45 %	Voltage=60 kV Power=6.5 W Time=**3h** Obj=0.4x Transmit=46 %	Voltage=100 kV Power=14 W Time=**7h** Obj=4x Transmit=52 %

Fig. 6. Schematic of the XCT set-up and the acquisition parameters for the various scans conducted in this study. The 3 mm coupon size scanned at a voxel size of 3.4 µm was considered as the 'ground truth'.

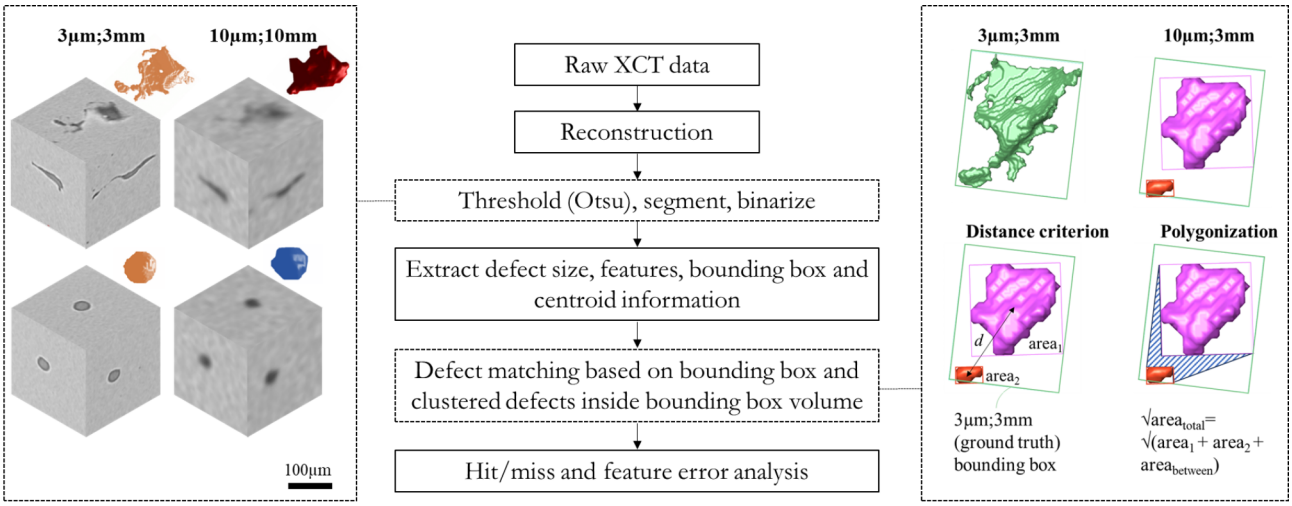

Fig. 7. Flowchart showing the procedure for XCT image processing, defect feature extraction and matching with the "ground truth" dataset for the POD and feature error analysis.

XCT post-processing, POD, and feature error analysis

The XCT projections were reconstructed in the Zeiss Reconstructor software. Following reconstruction, the images were segmented using Otsu thresholding to extract the defect features from the background material. All thresholded images were manually inspected to ensure the defect features were sufficiently captured. The binarized images were further processed in ORS Dragonfly software by despeckling and ensuring any CT image artifacts were removed for the porosity analysis. The 3D defects were labeled and several defect features including the volume, projected area, surface area, bounding box coordinates and centroid coordinates were obtained. A summary of the workflow is presented in Fig. 7 showing the methodology followed in this study for the POD and feature error analysis.

The various scans were aligned with the 'ground truth' dataset by translating, tilting, rotating and overlaying them on to the 'ground truth' scan so they occupied the same reference coordinate system. Defect centroids in the lower-resolution scans were then identified within the bounding box volume of the corresponding 'ground truth' defects. The hit/miss POD analysis followed guidelines from ASTM E2862 and MIL-HDBK-1823 A[28,46]. Since the objectives of this study pertained to the identification of defect features critical to fatigue loading scenarios, the projected $\sqrt{area}$ was selected as the size parameter for further analysis. In this work, the plane perpendicular to the build direction was selected as the projection plane. To quantify the POD, a defect was classified as a hit if it was detected within the bounding box of the 'ground truth' defect and, as a miss if no detection occurred within that bounding box. The hit/miss responses were plotted against the 'ground truth' defect sizes, with the miss data being assigned a POD of 0 and the hit data being assigned a POD of 1. The probit link function was used to generate the sigmoid POD curve and to obtain the probabilities from the binary outcomes, which is defined as follows:

$$Probit\ (\mathrm{POD}\,(\mathrm{a})) = \Phi^{-1}\,(\mathrm{POD}\,(\mathrm{a}))\,\#\,(1)$$

where Φ is the cumulative standard normal distribution and POD(a) is the probability of detection function with respect to size, a, of the defect.

The feature errors were analyzed by comparing various size features such as the volume, surface area and $\sqrt{area}$s between the low-resolution defect and the corresponding 'ground truth' defect. This allowed the measured $\sqrt{area}$ versus true $\sqrt{area}$ plots to be constructed[47]. In addition, it was observed that some of the lack of fusion defects appeared as a cluster of entities in the corresponding lower-resolution scans. This was a consequence of spatial resolution limitations, where the thin sections of the defects could not be resolved in the XCT images leading to multiple entities being detected, that belonged to the same defect as informed by the 'ground truth' scan. To address this and recover some of the lost information, a polygonization approach was proposed to estimate the area in between the cluster of defects that belonged to the same defect. The procedure involved calculating the distances between the pairwise entities in the low resolution scans and establishing a distance criterion to identify which entities were part of the same defect. The criterion for each resolution, was used to construct a convex hull using the bounding box coordinates of the clustered entities, allowing for the calculation of the projected areas as illustrated in Fig. 7.

Data availability

The XCT data are available under restricted access for having large size in the order of TBs, which cannot be stored or transferred on commonly available data sharing platforms. Access can be obtained by requesting from the corresponding author.

Code availability

Defect properties were extracted from XCT using ImageJ and Dragonfly Pro. Analysis of the results was performed using codes which can be accessed at https://doi.org/10.5281/zenodo.14510581.

Received: 12 February 2025; Accepted: 21 February 2025
Published online: 25 February 2025

References

1. Sanaei, N., Fatemi, A. & Phan, N. Defect characteristics and analysis of their variability in metal L-PBF additive manufacturing. *Mater. Des.* **182**, 108091 (2019).
2. Brandl, E., Heckenberger, U., Holzinger, V. & Buchbinder, D. Additive manufactured AlSi10Mg samples using selective laser melting (SLM): Microstructure, high cycle fatigue, and fracture behavior. *Mater. Des.* **34**, 159–169 (2012).
3. Ahmed, F. et al. Study of powder recycling and its effect on printed parts during laser powder-Bed fusion of 17-4 PH stainless steel. *J. Mater. Process. Technol.* **127177** https://doi.org/10.1016/j.jmatprotec.2019.116522 (2019).
4. Fatemi, A. et al. Fatigue behaviour of additive manufactured materials: An overview of some recent experimental studies on Ti–6Al–4V considering various processing and loading direction effects. *Fatigue Fract. Eng. Mater. Struct.* **42**, 991–1009 (2019).
5. Shamsaei, N., Yadollahi, A., Bian, L. & Thompson, S. M. An overview of direct laser deposition for additive manufacturing; part II: Mechanical behavior, process parameter optimization and control. *Addit. Manuf.* **8**, 12–35 (2015).
6. Stephens, R. I., Fatemi, A., Stephens, R. R. & Fuchs, H. O. *Metal Fatigue in Engineering* (Wiley, 2000).
7. Murakami, Y., Takagi, T., Wada, K. & Matsunaga, H. Essential structure of S-N curve: Prediction of fatigue life and fatigue limit of defective materials and nature of scatter. *Int. J. Fatigue* **146**, 106138 (2021).
8. Yadollahi, A. & Shamsaei, N. Additive manufacturing of fatigue resistant materials: Challenges and opportunities. *Int. J. Fatigue* **98**, 14–31 (2017).
9. Liu, W. et al. Study of pore defect and mechanical properties in selective laser melted Ti6Al4V alloy based on X-ray computed tomography. *Mater. Sci. Eng.: A* **797**, 139981 (2020).
10. Wu, Z. et al. The role of internal defects on anisotropic tensile failure of L-PBF AlSi10Mg alloys. *Sci. Rep.* **13**, 1–8 (2023).
11. Zhang, K. et al. Pore evolution mechanisms during directed energy deposition additive manufacturing. *Nat. Commun.* **15**(1), 1–14 (2024).
12. Sheridan, L., Scott-Emuakpor, O. E., George, T. & Gockel, J. E. Relating porosity to fatigue failure in additively manufactured alloy 718. *Mater. Sci. Eng.: A* **727**, 170–176 (2018).
13. Torries, B., Imandoust, A., Beretta, S., Shao, S. & Shamsaei, N. Overview on microstructure- and defect-sensitive fatigue modeling of additively manufactured materials. *Jom* **70**, 1853–1862 (2018).
14. Withers, P. J. X-ray nanotomography. *Mater. Today* **10**, 26–34 (2007).
15. du Plessis, A., Yadroitsava, I. & Yadroitsev, I. Effects of defects on mechanical properties in metal additive manufacturing: A review focusing on X-ray tomography insights. *Mater. Des.* **187**, 108385 (2020).
16. Thompson, A., Senin, N., Maskery, I. & Leach, R. Effects of magnification and sampling resolution in X-ray computed tomography for the measurement of additively manufactured metal surfaces. *Precis Eng.* **53**, 54–64 (2018).
17. du Plessis, A., Tshibalanganda, M. & le Roux, S. G. Not all scans are equal: X-ray tomography image quality evaluation. *Mater. Today Commun.* **22**, 100792 (2020).
18. Kim, F. H., Pintar, A. L., Moylan, S. P. & Garboczi, E. J. The influence of X-Ray computed tomography acquisition parameters on image quality and probability of detection of additive manufacturing defects. *J. Manuf. Sci. Eng. Trans. ASME* **141**, (2019).
19. Kastner, J., Harrer, B., Requena, G. & Brunke, O. A comparative study of high resolution cone beam X-ray tomography and synchrotron tomography applied to Fe- and Al-alloys. *NDT E Int.* **43**, 599–605 (2010).
20. Martin, A. A. et al. Dynamics of pore formation during laser powder bed fusion additive manufacturing. *Nat. Commun.* **10**(1), 1–10 (2019).
21. Cunningham, R. et al. Keyhole threshold and morphology in laser melting revealed by ultrahigh-speed x-ray imaging. *Science* **363**, 849–852 (2019).
22. Murakami, Y. *Metal Fatigue: Effects of Small Defects and Nonmetallic Inclusions*, vol. 47 (Elsevier, 2002).
23. Seifi, M. et al. Progress towards metal additive manufacturing standardization to support qualification and certification. *Jom* **69**, 439–455 (2017).
24. Niu, X. et al. Defect tolerant fatigue assessment of AM materials: Size effect and probabilistic prospects. *Int. J. Fatigue* **160**, 106884 (2022).
25. Macallister, N. & Becker, T. H. Fatigue life Estimation of additively manufactured Ti–6Al–4V: sensitivity, scatter and defect description in damage-tolerant models. *Acta Mater.* **237**, 118189 (2022).
26. Romano, S. et al. Fatigue properties of AlSi10Mg obtained by additive manufacturing: Defect-based modelling and prediction of fatigue strength. *Eng. Fract. Mech.* **187**, 165–189 (2018).
27. Akgun, E., Zhang, X., Lowe, T., Zhang, Y. & Doré, M. Fatigue of laser powder-bed fusion additive manufactured Ti–6Al–4V in presence of process-induced porosity defects. *Eng. Fract. Mech.* **259**, 108140 (2022).
28. Department of Defense. MIL-HDBK-1823A: Nondestructive Evaluation System Reliability Assessment. vol. 16. (2009).
29. Yosifov, M. et al. Probability of detection applied to X-ray inspection using numerical simulations. *Nondestruct. Test. Evaluat.* **37**, 536–551 (2022).
30. Kim, F. H. et al. Merging experiments and computer simulations in X-ray computed tomography probability of detection analysis of additive manufacturing flaws. *NDT E Int.* **119**, 102416 (2021).
31. Hu, Y. N. et al. The effect of manufacturing defects on the fatigue life of selective laser melted Ti–6Al–4V structures. *Mater. Des.* **192**, 108708 (2020).
32. Gordon, J. V. et al. Defect structure process maps for laser powder bed fusion additive manufacturing. *Addit. Manuf.* **36**, 101552 (2020).
33. Kasperovich, G., Haubrich, J., Gussone, J. & Requena, G. Correlation between porosity and processing parameters in TiAl6V4 produced by selective laser melting. *Mater. Des.* **105**, 160–170 (2016).
34. Poudel, A. et al. Feature-based volumetric defect classification in metal additive manufacturing. *Nat. Commun.* **13**, 1–12 (2022).
35. Brennan, M. C., Keist, J. S. & Palmer, T. A. Defects in metal additive manufacturing processes. *J. Mater. Eng. Perform.* **30**(7), 4808–4818 (2021).
36. Sundar, V. et al. Flaw identification in additively manufactured parts using X-ray computed tomography and destructive serial sectioning. *J. Mater. Eng. Perform.* **30**, 4958–4964 (2021).
37. Kerckhofs, G. et al. High-Resolution microfocus X-ray computed tomography for 3D surface roughness measurements of additive manufactured porous materials. *Adv. Eng. Mater.* **15**, 153–158 (2013).
38. Rodríguez-Sánchez, Á., Thompson, A., Körner, L., Brierley, N. & Leach, R. Review of the influence of noise in X-ray computed tomography measurement uncertainty. *Precis Eng.* **66**, 382–391 (2020).
39. Peng, X. et al. The potency of defects on fatigue of additively manufactured metals. *Int. J. Mech. Sci.* **221**, 107185 (2022).
40. Murakami, Y. & Endo, M. Effects of defects, inclusions and inhomogeneities on fatigue strength. *Int. J. Fatigue* **16**, 163–182 (1994).

41. Zerbst, U. et al. Damage tolerant design of additively manufactured metallic components subjected to cyclic loading: State of the art and challenges. *Prog Mater. Sci.* **121**, 100786 (2021).
42. NASA. NASA-STD-6030 Additive Manufacturing Requirements for Spaceflight Systems. (2021).
43. Rhein, R. K., Shi, Q., Tekalur, S. A., Jones, J. W. & Carroll, J. W. Short-Crack growth behavior in additively manufactured AlSi10Mg alloy. *J. Mater. Eng. Perform.* **30**, 5392–5398 (2021).
44. Di Giovanni, M. T., de Menezes, J. T. O., Bolelli, G., Cerri, E. & Castrodeza, E. M. Fatigue crack growth behavior of a selective laser melted AlSi10Mg. *Eng. Fract. Mech.* **217**, 106564 (2019).
45. Gorelik, M. Additive manufacturing in the context of structural integrity. *Int. J. Fatigue* **94**, 168–177 (2017).
46. ASTM. E2862-standard practice for probability of detection analysis for hit/miss data. **i**, 1–6. (2012).
47. ASTM. E3023-standard practice for probability of detection analysis for â versus a data, 1–6. https://doi.org/10.1520/E3023-21.2 (2012).

Acknowledgements

This work was partially supported by the National Institute of Standards and Technology (NIST) under Grant No. 70NANB22H084 and by the National Science Foundation (NSF) under Grant No. 2319690.

Author contributions

Conceptualization: S. Baig (S.B.), A.J., S.S., N.S.; Methodology: S. Baig (S.B.), A.J., S. Beretta (S.B.), S.S., N.S.; Investigation: S. Baig (S.B.), A.J., S. Beretta (S.B.), S.S., N.S.; Data Curation: S. Baig (S.B.); Formal analysis: S. Baig (S.B.), A.J., S. Beretta (S.B.), S.S., N.S; Writing-original draft: S. Baig (S.B.); Writing-review and editing: A.J., S. Beretta (S.B.), S.S., N.S.; Resources: S.S., N.S.; Supervision: N.S.; Project administration: N.S.; Funding acquisition: S.S., N.S.

Declarations

Competing interests

The authors declare no competing interests.

Additional information

Supplementary Information The online version contains supplementary material available at https://doi.org/10.1038/s41598-025-91608-6.

Correspondence and requests for materials should be addressed to N.S.

Reprints and permissions information is available at www.nature.com/reprints.

Publisher's note Springer Nature remains neutral with regard to jurisdictional claims in published maps and institutional affiliations.